Development of a position–velocity–time-modulated two-dimensional ion beam figuring system for synchrotron x-ray mirror fabrication

Tianyi Wang,[1,*] **Lei Huang,**[1] **Yi Zhu,**[1] **Matthew Vescovi,**[1] **Denis Khune,**[1] **Hyukmo Kang,**[2] **Heejoo Choi,**[2] **Dae Wook Kim,**[2] **Kashmira Tayabaly,**[1] **Nathalie Bouet,**[1] **and Mourad Idir**[1]

[1]*National Synchrotron Light Source II (NSLS-II), Brookhaven National Laboratory, PO Box 5000, Upton, New York 11973, USA*
[2]*James C. Wyant College of Optical Sciences, University of Arizona, 1630 E. University Blvd., P.O. Box 210094, Tucson, Arizona 85721-0094, USA*
Corresponding author: tianyi@bnl.gov

With the rapid evolution of synchrotron x-ray sources, the demand for high-quality precision x-ray mirrors has greatly increased. Single nanometer shape accuracy is required to keep imaging capabilities at the diffraction limit. Ion beam figuring (IBF) has been used frequently for ultra-precision finishing of mirrors, but achieving the ultimate accuracy depends on three important points: careful alignment, accurate dwell time calculation and implementation, and accurate optical metrology. The Optical Metrology Group at National Synchrotron Light Source II has designed and built a position–velocity–time-modulated two-dimensional IBF system (PVT-IBF) with three novel characteristics: (1) a beam footprint on the mirror was used as a reference to align the coordinate systems between the metrology and the IBF hardware; (2) the robust iterative Fourier transform-based dwell time algorithm proposed by our group was applied to obtain an accurate dwell time map; and (3) the dwell time was then transformed to velocities and implemented with the PVT motion scheme. In this study, the technical aspects of the PVT-IBF systems are described in detail, followed by an experimental demonstration of the figuring results. In our first experiment, the 2D RMS in a 50 mm × 5 mm clear aperture was reduced from 3.4 to 1.1 nm after one IBF run. In our second experiment, due to a 5 mm pinhole installed in front of the source, the 2D RMS in a 50 mm × 5 mm clear aperture was reduced from 39.1 to 1.9 nm after three IBF runs, demonstrating that our PVT-IBF solution is an effective and deterministic figuring process. © 2020 Optical Society of America

https://doi.org/10.1364/AO.389010

1. INTRODUCTION

As EUV lithography and the third and fourth generation x-ray synchrotron sources evolve, the smoothness and precision of x-ray mirrors have dramatically increased. Surface profiles often need to reach single nanometer accuracy to avoid destruction of the incoming wave front or keep imaging capabilities at the diffraction limit [1,2]. Such a high level of surface quality, however, cannot be easily achieved by conventional mechanical polishing techniques.

Ion beam figuring (IBF) is one of the best deterministic methods for optical surface finishing and has been used frequently for creating ultra-precision mirrors [3–8]. IBF removes material from an optical surface at atomic level by physical sputtering. It has many advantages over conventional mechanical polishing methods [3,6,8]. For example, it is a highly deterministic and non-contact process. It is completely computer controlled and

requires no mechanical load force on the surface, so there is essentially no surface or sub-surface damage. In addition, edge effects are low, and the final surface is free of any process residue. These attractive features motivated us to build our own IBF system. We are excited to notice that our colleagues at Diamond Light Source (DLS) are following the same path and are also building their IBF system [9].

We started our initial IBF research by designing and integrating the one-dimensional IBF (1D-IBF) capability into an existing deposition chamber that was initially developed to fabricate multilayer Laue lenses (MLLs) for hard x-ray nanofocusing [3,10]. Our preliminary research works have demonstrated the figuring results of both flat and spherical grazing incidence reflective mirrors [3,7,8]. The figure errors of the flat mirrors were reduced to <1 nm RMS, while the spherical mirror's surface was improved from 21.5 nm RMS to 1.4 nm RMS [8]. In parallel, a new slope-based figuring

method was proposed to fit the slope measuring equipment [7]. Recently, the 1D-IBF process was further improved with a new alignment method and a more robust dwell time algorithm [6]. Sub-nanometer RMS convergence for both flat and spherical mirrors was achieved. It is worth noting that our initial tests were to polish mirrors in 1D. However, there is now an increasing demand to correct the surface in 2D for some x-ray applications. As an example, beamlines at National Synchrotron Light Source II (NSLS-II) utilize a variety of x-ray mirrors of different shapes and sizes. They are always non-planar and have different shapes and accuracy requirements in the tangential and sagittal directions. This consideration will be more stringent with the newly developed diffraction limited storage ring.

Using our experience from the development of our 1D-IBF, we began in early 2018 to build our own 2D-IBF system (see Fig. 1). Achieving the ultimate accuracy in 2D is even more challenging and depends on many factors, such as repeatable alignment of coordinate systems when transferring the mirror from IBF to metrology instruments, accurate dwell time calculation and its appropriate implementation, accurate optical metrology, etc. In this paper, we describe in detail the development of our position–velocity–time-modulated 2D-IBF system (PVT-IBF), including the system specifications, fine tuning of the motion stages, and stability tests of the ion beam, and then the experimental figuring results are demonstrated. The success of the proposed PVT-IBF depends on three critical aspects.

First, as IBF must be performed in high vacuum, *ex situ* measurement of the sample mirror is preferred. However, alignment errors exist in transferring the mirror between the IBF system and the metrology instrument. Therefore, in this study, a beam footprint on the mirror was used as a reference to align the coordinate systems between the metrology and the PVT-IBF hardware. The dwell time calculation is another difficulty in the IBF method, since it is modeled as an ill-posed deconvolution process and thus may not have a unique solution. Besides the non-negativity, a reasonable dwell time solution should duplicate the shape of the desired removal map, and the estimated residual should be small. In our 1D-IBF work, we have proposed an improved matrix-based method called constrained linear least-squares (CLLS) that automatically fulfills these requirements [6]. However, any algebraic methods [11,12] may fail in 2D due to limited memory space and long computation time. The more efficient frequency-domain methods [13,14] using Fourier transform are thus preferred. Specifically, an optimized robust iterative Fourier transform-based dwell time algorithm (RIFTA) [15,16] proposed by our group was applied to the 2D dwell time calculation. Third, smooth and accurate dwell time implementation is also critical to obtain expected figuring results. In this study, the calculated dwell time map was transformed to the velocity map and implemented with the PVT control scheme.

With these considerations, two experiments have been successfully performed using the PVT-IBF system. The measurement instrument used in this study is a 6-inch Zygo Verifire HD Fizeau interferometer (lateral resolution 0.13 mm/pixel). In our first proof of principle experiment, the 2D RMS in a 50 mm × 5 mm planar clear aperture (CA) was reduced from 3.4 to 1.1 nm after one IBF run, even though a wide 24 mm diameter ion beam was used. In the second experiment, the 2D

RMS in a 50 mm × 5 mm planar CA was reduced from 39.1 to 8.8 nm with the same 24 mm diameter ion beam after one IBF run. A 5 mm pinhole was then installed in front of the ion source, and the final 2D RMS achieved 1.9 nm after two more IBF runs.

The rest of the paper is organized as follows. Section 2 introduces the PVT-IBF system specifications. In Section 3, the system parameters such as the motion system accuracy and the ion beam stability are studied and tuned. Section 4 describes the three strategies applied to the PVT-IBF and demonstrates the experimental figuring results. Discussion and future work are given in Section 5. Section 6 concludes the paper.

2. DESCRIPTION OF THE NSLS-II PVT-IBF SYSTEM

A. Air-Side Components

The PVT-IBF system, as shown in Fig. 1(a), is composed of a 1.0 m × 0.6 m × 0.6 m vacuum chamber. The combination of an nXDS10i rough pump and an ETC1104 turbo-molecular pump (which is mounted on the top of the chamber) provides a base pressure of $\leq 1.0 \times 10^{-6}$ Torr. The working pressure (generally $\leq 5 \times 10^{-4}$ Torr) is achieved by adjusting the position of a motorized gate valve between the turbo pump and the chamber while injecting gas into the chamber. The chamber pressure is monitored by three pressure gauges, including two KJL275 convection gauges (CGs) and one KJLC351 ionization gauge.

B. In-Vacuum Components

The main in-vacuum components, as shown in Figs. 1(b) and 1(c), are the ion source, motion stages, and the mirror holder.

A Kaufman & Robinson (KRi) KDC10 ion source is used for the IBF process. It emits a circular-shaped ion beam with diameter ≤ 12 mm at the grid with self-aligned focused ion optics. A LFN1000 external neutralizer is mounted below the KDC10 to emit electrons to compensate for the space charge generated by the ion beam. Both the KDC10 and LFN1000 are fed with high-purity argon ($\geq 99.999\%$) via mass flow controllers (MFCs), which are controlled by the Kaufman Source Controller (KSC) ion source controller and the Integrated Neutralizer Controller (INC) neutralizer controller, respectively.

In this PVT-IBF system, the ion beam moves, whilw the mirror stays fixed. This design saves space in the chamber, and the mirror holder shown in Fig. 1(c) can hold a mirror up to 450 mm in length. The KDC10 and LFN1000, as shown in Fig. 1(b), are mounted to three-axis in-vacuum translation stages. The primary axis, which scans in the horizontal direction, uses a Newmark NLS8 linear stage with a travel range of 500 mm. The vertical scan and the motion along the ion beam's axis are achieved by two NLE-50 linear stages, each of which has a 50 mm travel range. All three linear stages are equipped with stepper motors and precise encoders with 0.1 μm resolution. The motion of the stages is controlled by a NSC-G3-E-41X controller, which is equipped with a DMC-41 × 3 motion card that supports PVT control mode.
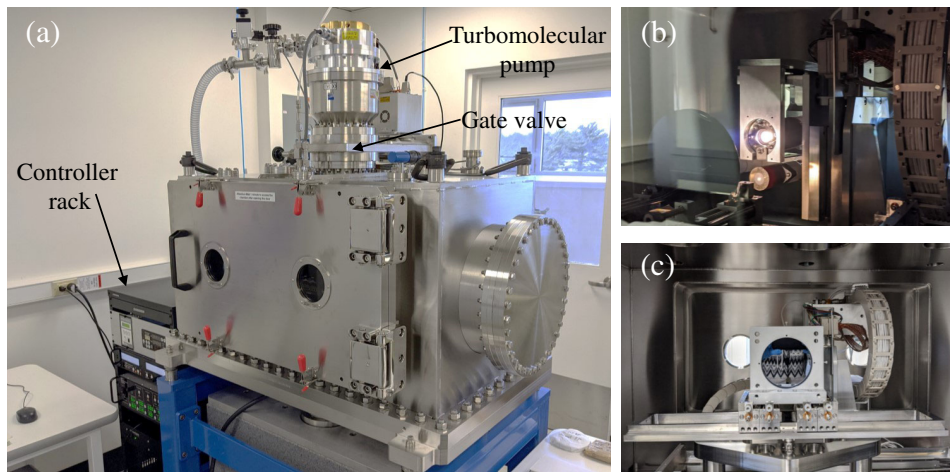
Fig. 1. (a) PVT-IBF chamber and the control rack. (b) KRi KDC10 ion source and LFN1000 neutralizer. (c) Adjustable holder for mirrors.
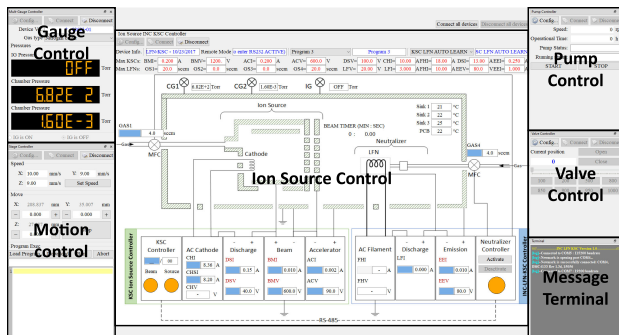
Fig. 2. PVT-IBF system is computer controlled by the self-developed software.

C. Software

As shown in Fig. 2, the operations of the various electrical components of the PVT-IBF system are integrated into a PC software specifically designed and developed by our group. The PC communicates with each of the controllers via its RS232 port. Execution status is monitored in real time when processing. Errors from one component will be broadcasted to all the others so that the entire PVT-IBF system can respond and stop the process when and if necessary.

## 3. STUDY OF THE SYSTEM PARAMETERS

Motion accuracy and ion source stability are the two most essential parameters in a fully functional PVT-IBF system. In the following two subsections, the dynamic performance of the primary horizontal translation stage is studied and tuned, followed by a presentation of the stability test of the ion source.

A. Motion Error Analysis and Compensation for the Primary Translation Stage

The motion accuracy of the primary stage is crucial for positioning the ion beam at correct dwell positions. As the PVT motion mode is used for smooth dwell time implementation (see Section 4), the motion error using PVT for the middle

400 mm of the primary stage is studied with the experiment designed and conducted as below.

First, the middle 400 mm travel range is subdivided into 1 mm displacement steps, which are analogous to the real PVT-IBF processing interval. Therefore, there are 800 steps in total

Forward error STD = 1.8663 μm, Backward error STD = 2.0297 μm
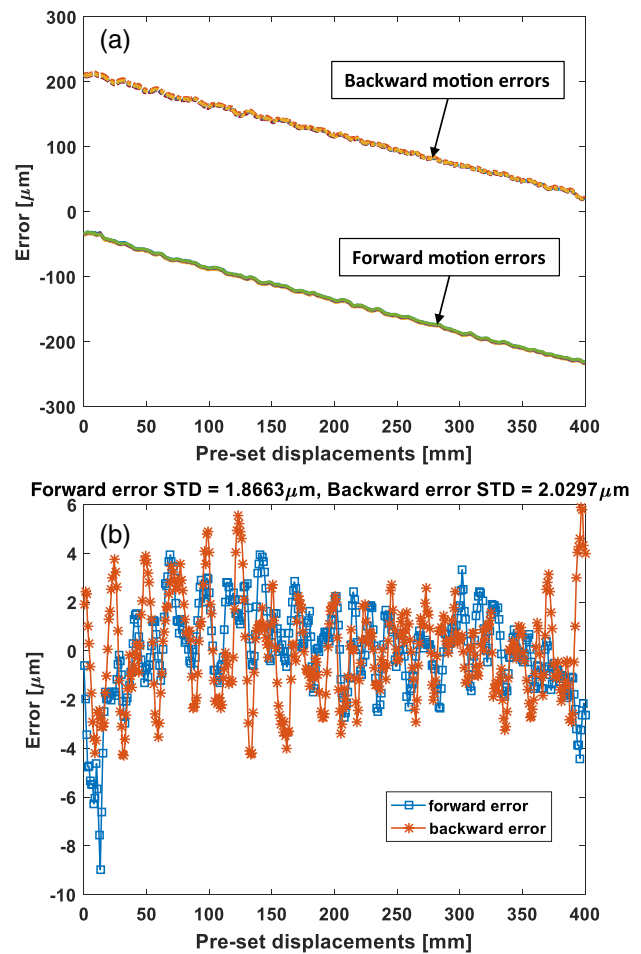
Fig. 3. (a) Linear errors exist in both the forward and backward PVT motions of the primary stage. (b) Errors become random after removing the linearity.

for a round of forward and backward displacements. Afterwards, the relative positions and end velocities of the PVT commands for each step are set to 1 mm and 0 mm/s, respectively. The current position of the stage is read from the encoder and recorded after completing each motion step. The above procedure is repeated for five rounds, and the motion time of the PVT commands for one step in each round is set to 0.0625 s, 0.125 s, 0.5 s, 1 s, and 2 s, respectively.

Figure 3(a) plots the errors between the pre-set and the measured displacements in the abovementioned five rounds of forward and backward motions. It can be found that both the forward and backward motion errors are linear, and a constant backlash exists when changing the motion direction. After compensating for the linearity and removing the backlash, as shown in Fig. 3(b), the expected random errors have standard deviations (STDs) around 2 μm, which is good enough for the PVT-IBF with the 1 mm processing interval.

The dynamic performance of the primary stage is then tuned with this linearity and backlash compensation. The linearity is removed by multiplying the counts sent to the stepper motor by the coefficient calculated from Fig. 3(a). The constant forward and backward backlashes are compensated for by an iterative algorithm. Using the encoder reading as a reference, the algorithm keeps finding the additional counts that should be sent to the motor until the difference between the expected position and the encoder reading is less than 5 μm. The effectiveness of this fine tuning is verified in Fig. 4, in which the tests are
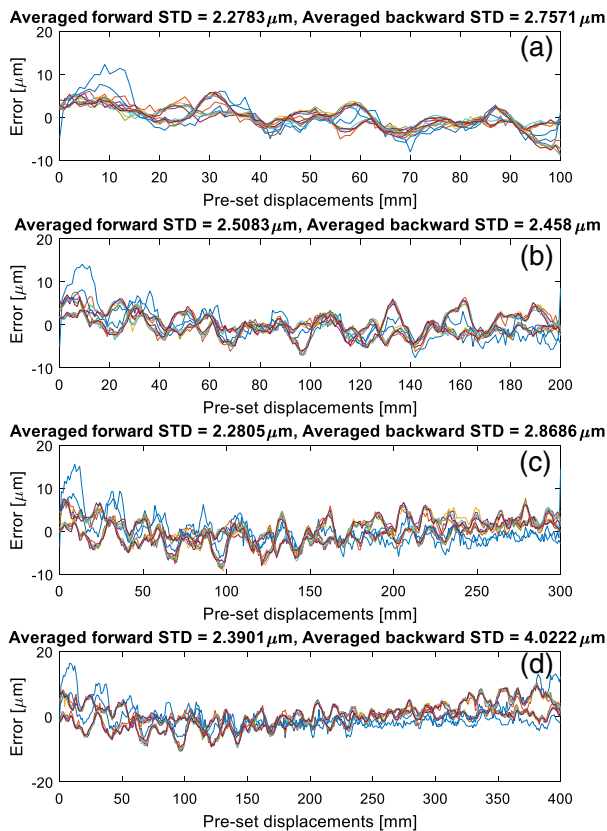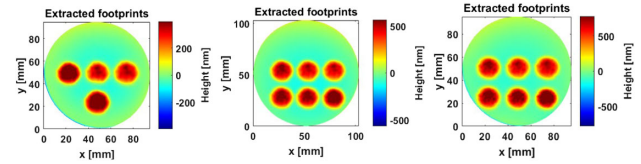
Fig. 5. Sixteen ion beam footprints bombarded at different distances from the ion source grid to the mirror surface. The dwell time used to bombard each footprint is 5 min.

performed on four travel ranges of 100 mm [Fig. 4(a)], 200 mm [Fig. 4(b)], 300 mm [Fig. 4(c)], and 400 mm [Fig. 4(d)]. For each test, seven rounds of forward and backward motions with 1 mm displacement steps and 0 mm/s end velocities are performed. The motion time for one step in each round is set to 0.0625 s, 0.125 s, 0.25 s, 0.5 s, 1 s, and 2 s, respectively. The averaged STDs of the forward and backward motion errors indicate that the fine-tuning results of the primary stage coincide with the prediction shown in Fig. 3(b), and its forward dynamic performance is higher than its backward counterpart. Also, a better accuracy is obtained at a shorter travel range.

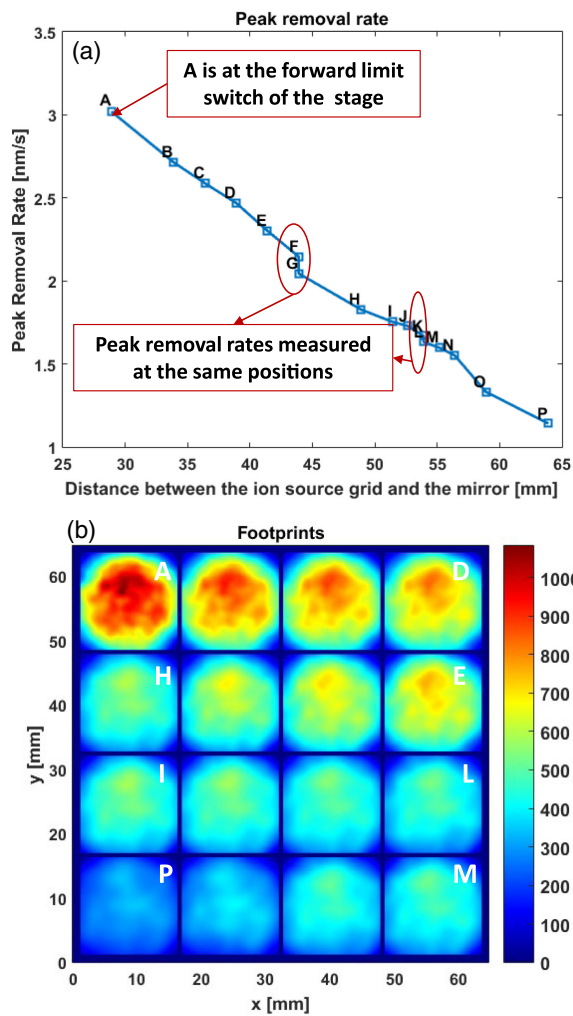## B. Stability Test of the Ion Source

1. Static Stability of the Ion Source

Ion beam stability is crucial for the deterministic process. In this study, the ion beam's peak removal rate (PRR) and its shape are examined by extracting the bombarded footprints on test mirrors. Starting from a distance of 28.9 mm from the ion source grid to the mirror surface, the ion source is translated away from the mirror. After each translation, a footprint is bombarded for 5 min on the mirror surface.

As shown in Fig. 5, totally 16 footprints are bombarded onto three flat circular silicon mirrors. The PRR of each footprint is calculated using a 2D Gaussian fit with a 15 mm diameter, and the fitting results versus distances from the ion source grid to the mirror surface are shown in Fig. 6(a). The corresponding shapes of the extracted ion beam footprints are given in Fig. 6(b). It can be found that the PRR is linear with respect to the distance, and the intensity distribution of the ion beam remains constant. It is also worth mentioning that the points labeled "F" and "G" as well as "K" and "L" in Figs. 6(a) and 6(b) are measured at the same ion source to mirror surface distances. The differences between their PRRs and shapes are so small that they can be ignored. This indicates that the ion source is very stable, and its footprint does not have to be reevaluated if its location is fixed and the ion beam voltage and current remain invariant. In this study, the ion source is finally fixed at the location of K and L with a PRR of about 2 nm/s.

2. Dynamic Stability of the Ion Source

As verified in the above experiment, the ion source is stable. However, the ion source stability during translation is affected by another two factors, namely, the vibration of the translation stage and the possible tilt angle between the ion source and the mirror surfaces. The dynamic stability is thus further studied by scanning a trench [17] on the surface of a mirror in the primary direction. As shown in Fig. 7(a), the ion source is moved forward
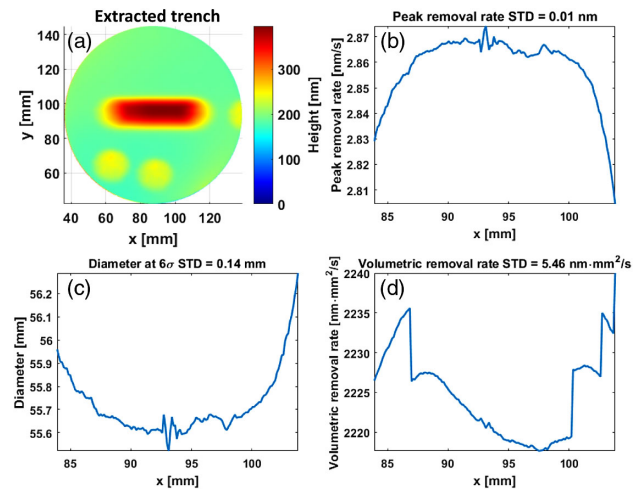

Fig. 4. Forward and backward motion errors for the travel ranges of (a) 100 mm, (b) 200 mm, (c) 300 mm, and (d) 400 mm after compensation for linearity and backlash.

Fig. 6. Peak removal rates (a) for the 16 ion beam footprints (b) at different distances from the ion source grid to the mirror surface.

Fig. 7. (a) One trench and two ion beam footprints bombarded on a flat circular mirror. (b) Peak removal rate, (c) diameter of the ion beam, and (d) volumetric removal rate are learned by fitting the middle 20 mm of the trench with a 1D Gaussian in y direction.

and backward with a constant speed of 1 mm/s on the center 50 mm range of a circular mirror along the x axis. Three rounds of the forward and backward translations are performed, so the total scanning time is approximately 5 min.
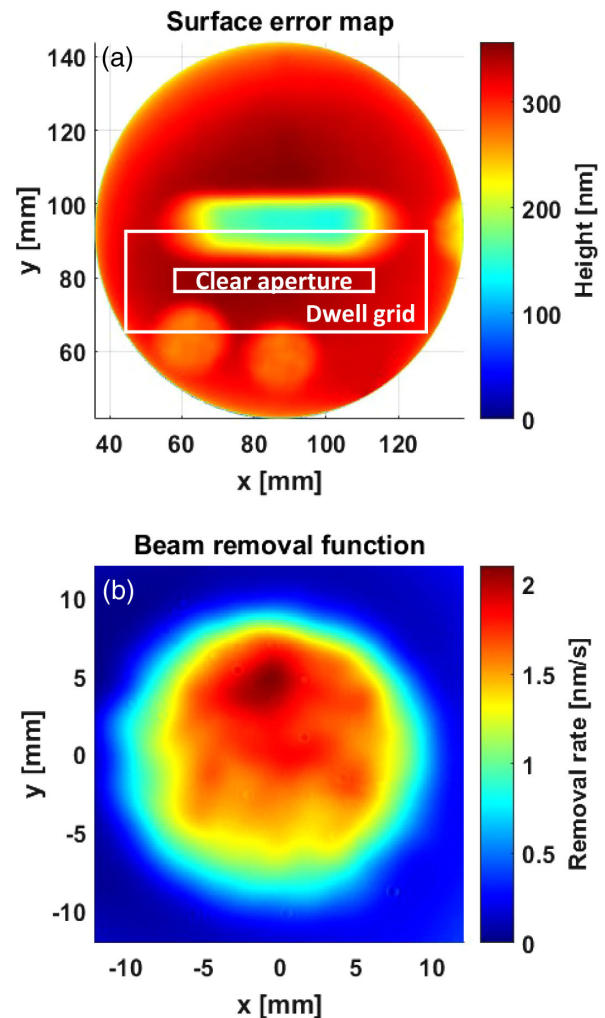
The cross sections of the 84 to 104 mm range of the trench along the x axis are fitted with a 1D Gaussian. The learned PRRs, ion beam diameter, and volumetric removal rates (VRRs) are shown in Figs. 7(b), 7(c), and 7(d), respectively, the STDs of which are only 0.01 nm, 0.14 mm, and 5.46 nm · mm^2/s. These experimental results indicate that the ion source is also stable during its translation. The vibration of the translation stage is negligible, and the ion source and the mirror surfaces are perfectly parallel to each other.

## 4. PVT-IBF STRATEGIES AND EXPERIMENTS

Two experiments have been successfully performed using the PVT-IBF system. The three critical strategies of achieving the initial success are described in detail based on the first experiment. The same strategies are applied to the second experiment.

Fig. 8. (a) Surface height map of the mirror for the first experiment. (b) Beam removal function extracted from the footprints.
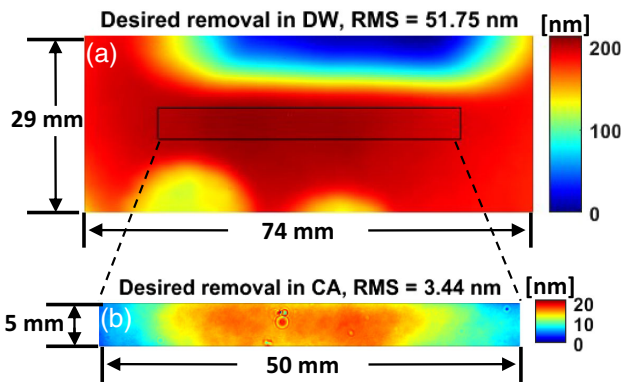
Fig. 9. (a) Desired removal height in dwell grid and (b) desired removal height in clear aperture for the first experiment. The RMS values are calculated in 2D.

In addition, a 5 mm pinhole is installed in front of the ion source to reduce the ion beam footprint and increase its figuring capability.

In the first experiment, the same mirror shown in Fig. 7(a) is used. In the PVT-IBF process, as shown in Fig. 8(a), a CA is specified below the scanned trench. Since IBF has no over-hang problem, the CA is usually enclosed in a dwell grid (DG), which is usually larger than CA with the radius of the beam removal function (BRF) on each side [6,11–14]. In this experiment, as shown in Fig. 9, the CA size is 5 mm × 50 mm. The BRF diameter is 24 mm [see Fig. 8(b)], so the DG size is 29 mm × 74 mm.

A. Calibration of the Coordinate Systems of the Interferometer and the PVT-IBF System

The *ex situ* metrology of the mirror surface is performed using a Zygo Verifire interferometer. Accurate calibration between the coordinate systems of the interferometer and the PVT-IBF system is essential for the success of the figuring process. This is done using ion beam footprints as reference markers on the mirror when it is transferred between the two instruments.

As shown in Fig. 8(a), two ion beam footprints are bombarded onto the mirror outside the CA, each with 30 s dwell time. The encoder values of the translation stages are recorded as $[x_{ibf}, y_{ibf}]$, which represent the coordinates of the footprint centers in the PVT-IBF coordinate system. The surface maps before and after the bombardment are measured by the interferometer. The subtracted surface error map is then fitted to a 2D Gaussian. The fitted footprint centers are recorded as $[x_m, y_m]$ in the interferometer's coordinate system. The coordinates' correspondence is thus constructed with $[x_{ibf}, y_{ibf}]$ and $[x_m, y_m]$. The CA range is defined in interferometer's coordinate system with respect to $[x_m, y_m]$. The same relative relationship between the CA and $[x_m, y_m]$ can be used to determine the CA in the PVT-IBF system. Another advantage of this calibration method is that the BRF (see Fig. 8) can be extracted at the same time without using a Faraday cup detector.

B. Dwell Time Calculation

1. Principle

In IBF, the removed height $Z(x, y)$ is modeled as the con-volution between the BRF $B(x, y)$ and the dwell time map $T(x, y)$ as

$$Z(x, y) = B(x, y) * T(x, y). \tag{1}$$

$Z(x, y)$ and $B(x, y)$ are known, and $t(x, y)$ can be estimated by deconvolution, which is an ill-posed inverse problem and may not have a unique solution [11,12].

2. Dwell Time Algorithms

Dwell time algorithms can be divided into two categories [16]. One category is frequency-domain methods using Fourier transform [13–15]; the other category is matrix-based methods [6,11,12,18], which discretize Eq. (1) in matrix form as

$$Z(x_k, y_k) = \sum_{i=1}^{N_t} B(x_k - \xi_i, y_k - \eta_i) T(\xi_i, \eta_i), \tag{2}$$

where N_t is the total numbers of dwell positions, $B(x_k - \xi_i, y_k - \eta_i)$ is the material removal amount per unit time at (x_k, y_k) when the beam dwells at (ξ_i, η_i), and $T(\xi_i, \eta_i)$ is the dwell time. While the frequency-domain methods must be performed on the entire DG, the matrix-based methods can use just the CA information. In other words, $Z(x_k, y_k)$ in Eq. (2) is the CA in matrix-based methods. This brings the advantage that the dwell time solution is not influenced by the shape outside the CA. However, the computational burden of the matrix-based methods is much heavier than the frequency-domain ones.

In this study, the performances of both a frequency-domain method using the Bayesian updates [13] and a matrix-based method using least squares with QR-factorization(LSQR) [12] are tested on the DG and the CA shown in Fig. 9. The calculated dwell time maps are given in Figs. 10(a) and 10(c), and the corresponding estimated residual maps in the CA are shown in Figs. 10(b) and 10(d). The dwell time map obtained by the Bayesian method closely duplicates the shape of the DG. The estimated residual in the CA, however, is higher than that calculated using LSQR, since the Bayesian method is affected by the three low areas in the DG. It can be noted that the dwell time map calculated by LSQR hardly duplicates the shape of DG. Therefore, both the Bayesian method and LSQR failed to provide a robust dwell time solution in this case.

3. RIFTA Dwell Time Algorithm

Recently, we have proposed the RIFTA algorithm [15,16], which combines the advantages of both the frequency-domain methods and matrix-based methods. The RIFTA method uses the efficient fast Fourier transform (FFT) to perform deconvo-lution. Moreover, instead of the entire DG, the RIFTA uses only the estimated residuals in the CA to iteratively update the dwell time map.

The initial purpose of the RIFTA is to achieve non-negativity and reduce the total dwell time at the same time. Suppose that
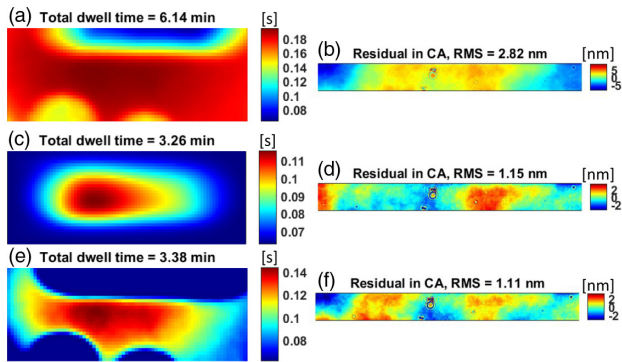
Fig. 10. (a), (c), (e) Calculated dwell time maps and (b), (d), (f) corresponding estimated residual maps in CA using (a), (b) the Bayesian method , (c), (d)TSVD , and (e), (f) RIFTA.

the desired removal in the DG is $Z_d(x, y)$. In each inner-iteration of the RIFTA, $Z_d(x, y)$ is adjusted by a piston equal to the minimum estimated residual value in the CA. The negative entries in the calculated $T(x, y)$ are set to zeros. As a result, it is always guaranteed that $Z_d(x, y)$ is adjusted by the smallest (i.e., optimal) piston during the iterative calculations. These iterations are performed until the STD difference of the difference between the current and the previous estimated residual maps in the CA is less than a threshold. To further reduce the total dwell time, an outer-iteration is added to minimize the DG size. This is specifically helpful when the desired removal amount is large and the total dwell time is still too long.

More details of the RIFTA algorithm can be found in Ref. [15,16]. Furthermore, in Ref. [16], the performances of different dwell time algorithms [6,11–15,18] were compared with our proposed RIFTA by simulation, showing that the RIFTA is superior to the other algorithms in that it consumes shorter total dwell time to achieve equally good or even smaller estimated residual maps in the CA.

The dwell time map calculated using the RIFTA in Fig. 9 is given in Fig. 10(e), and the corresponding estimated residual map is shown in Fig. 10(f). It is obvious that in addition to the advantages mentioned above, the RIFTA automatically avoids the low areas in the DG. The estimated residual map is also the best of the three methods. Thus, the dwell time map calculated using the RIFTA is used in this experiment.

C. Dwell Time Implementation with PVT Motion Control

The smooth implementation of the calculated dwell time map is also crucial for obtaining desired figuring results. Conventionally, the dwell time map is implemented in a position-based way such that the ion beam is moved to each machining point and kept at that point for the entire dwell time. This implementation is not smooth and increases the total process time. In this study, the calculated dwell time is transformed into velocities along the primary horizontal axis [19] and scheduled using PVT commands, while the raster scan is performed in the vertical direction. The velocity mode smooths the motion of the stages and saves the total process time, which is specifically important when the total dwell time is long.
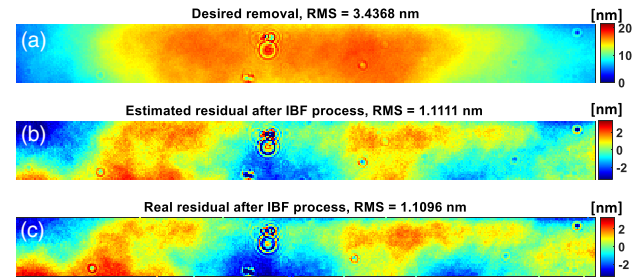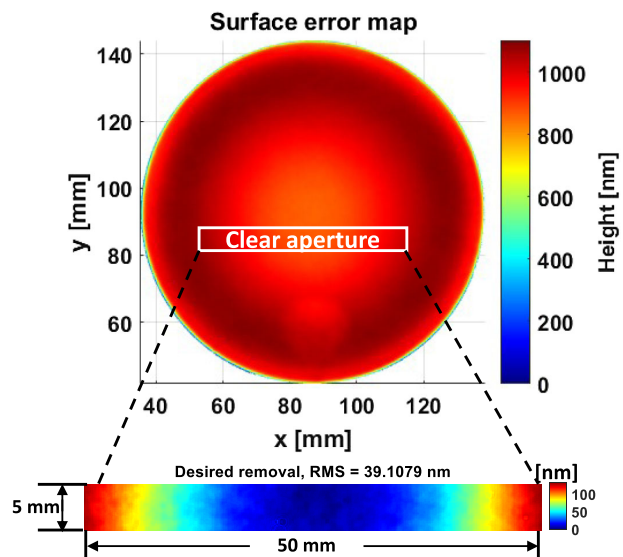

Fig. 11. (a) Desired removal map in the CA. (b) Estimated residual map in the CA. (c) Real residual map in the CA after one PVT-IBF run.

D. Experimental Results

The experiments that apply the three aspects described above are performed on two silicon mirrors using the PVT-IBF system. The following operational parameters are used for the KDC10 and the LFN1000: beam voltage, $V_b = 600$ V; beam current, $I_b = 10$ mA; accelerator voltage, $V_a = -90$ V; accelerator current, $I_a = 2$ mA; and LFN emission current, $I_e = 10$ mA.

In the first experiment, after one run of the PVT-IBF process on the CA shown in Fig. 11(a), the residual shape error in the CA is shown in Fig. 11(c). The obtained 2D RMS is 1.11 nm, as expected in our simulation estimation shown in Fig. 11(b). In addition, the shapes of the estimation and the real residual map in CA are very similar to each other.

In the second experiment, as shown in Fig. 12, the desired removal map in the 5 mm × 50 mm CA has a 2D RMS of 39.1 nm. Initially, the same BRF shown in Fig. 8(b) is used, and the estimated 2D RMS of the residual in the CA is 3.4 nm, which is limited by the figuring capability of the BRF. The figuring result is presented in Figs. 13(a) and 13(b), in which the 2D RMS of the residual in the CA is improved from 39.1 to 8.8 nm with 13 min total dwell time. The discrepancy between the estimation and the real figuring result further indicates that the limit of the figuring capability of the BRF is reached. In order to improve the IBF capabilities, a 5 mm diameter pinhole

Fig. 12. Surface error map and the desired removal map in the CA for the second experiment.
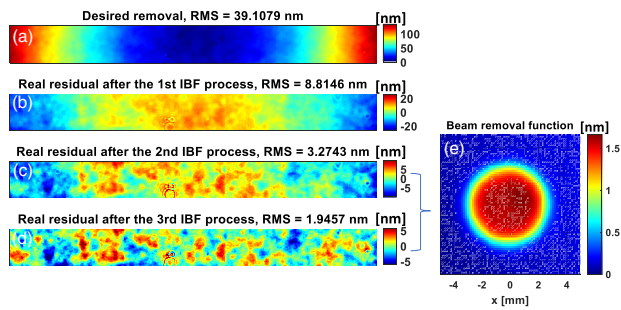
Fig. 13. (a) Desired removal map in the CA. (b) Residual map in the CA after the first PVT-IBF process using the 24 mm diameter BRF. (c) Residual map in the CA after the second PVT-IBF process using the 10 mm diameter BRF. (d) Residual map in the CA after the third PVT-IBF process using the 10 mm diameter BRF. (e) BRF generated by placing a 5 mm diameter pinhole in front of the ion source.

made of pyrolytic graphite was added at a distance of 30 mm from the ion source surface to reduce the ion beam footprint and increase its removal capability at a higher frequency. The new focused BRF is shown in Fig. 13, which is more uniform on each side and has higher energy density in the middle. As shown in Figs. 13(c) and 13(d), the final 2D RMS of the residual in the CA achieves 1.9 nm after two IBF runs using the focused BRF. The two experiments demonstrated above prove that the PVT-IBF system is an effective and deterministic figuring process.

The roughness of the mirrors both before and after the PVT-IBF process was measured using a Zygo New View white-light microscope interferometer. Five points of interest located in each of the CAs in the two mirrors are measured. The RMS roughnesses before and after the PVT-IBF process for the first experiment are 0.30 nm, 0.31 nm, 0.34 nm, 0.30 nm, and 0.33 nm versus 0.31 nm, 0.32 nm, 0.32 nm, 0.32 nm, and 0.33 nm. For the second experiment, the results are 1.42 nm, 1.50 nm, 1.55 nm, 1.50 nm, and 1.50 nm versus 1.41 nm, 1.54 nm, 1.54 nm, 1.50 nm, and 1.50 nm, which demonstrates that the surface roughness of the mirror is almost not affected by the PVT-IVF process.

5. DISCUSSION AND FUTURE WORK

The current PVT-IBF system achieves the level of 1 nm 2D RMS convergence corresponding to the interferometric measurement results, and the real figuring performances well match our estimations. The total dwell time ranges from 3 to 13 mins, and the maximum figure error corrected is 39.1 nm 2D RMS. However, for high-precision synchrotron x-ray mirrors, sub-nanometer RMS convergence is preferred.

Following our presented PVT-IBF system development and the initial successful figuring experiments, the primary objective will be to install an adjustable pinhole in front of the ion source to flexibly focus and filter the beam to tune its figuring capability when and if necessary. Figuring of higher-precision x-ray mirrors will then be attempted. Since these mirrors are long and often have rectangular shape, the stitching interferometry platform recently developed [20] in our lab will be used as the key metrology instrument.

6. CONCLUSION

A PVT-IBF has been designed and built at the NSLS-II. The technical aspects of the system such as the dynamic performances of the translation stages and the stability of the ion source are presented. Figuring experiments on two 5 mm × 50 mm CA mirrors are then successfully performed. The positive results are attributed to three critical aspects. First, the ion beam footprints on the mirror are used as reference markers to align the coordinate systems of the interferometer and the PVT-IBF system. Second, the RIFTA is applied to obtain an accurate dwell time map. Third, the dwell time map is then transformed into a velocity map and implemented with the PVT control mode. The 2D RMS in the CA in the first experiment is reduced from 3.4 to 1.1 nm and well fits the estimation. In the second experiment, a 5 mm pinhole is placed in front of the ion source to reduce the ion beam footprint and increase its figuring capability. After three PVT-IBF processes, the 2D RMS is reduced from 39.4 to 1.9 nm. The experimental results indicate that the PVT-IBF is an effective and deterministic figuring process that can be used to process higher-precision synchrotron x-ray mirrors.

Disclosures. The authors declare no conflicts of interest.

REFERENCES

1. K. Yamauchi, H. Mimura, T. Kimura, H. Yumoto, S. Handa, S. Matsuyama, K. Arima, Y. Sano, K. Yamamura, K. Inagaki, H. Nakamori, J. Kim, K. Tamasaku, Y. Nishino, M. Yabashi, and T. Ishikawa, "Single-nanometer focusing of hard x-rays by Kirkpatrick–Baez mirrors," J. Phys. Condens. Matter **23**, 394206 (2011).
2. K. Yamauchi, H. Mimura, S. Matsuyama, H. Yumoto, T. Kimura, Y. Takahashi, K. Tamasaku, and T. Ishikawa, "Focusing mirror for coherent hard x-rays," in *Synchrotron Light Sources and Free-Electron Lasers: Accelerator Physics, Instrumentation and Science Applications*, E. Jaeschke, S. Khan, J. R. Schneider, and J. B. Hastings, eds. (Springer, 2016).
3. M. Idir, L. Huang, N. Bouet, K. Kaznatcheev, M. Vescovi, K. Lauer, R. Conley, K. Rennie, J. Kahn, R. Nethery, and L. Zhou, "A one-dimensional ion beam figuring system for x-ray mirror fabrication," Rev. Sci. Instrum. **86**, 105120 (2015).
4. I. Preda, A. Vivo, F. Demarcq, S. Berujon, J. Susini, and E. Ziegler, "Ion beam etching of a flat silicon mirror surface: a study of the shape error evolution," Nucl. Instrum. Methods Phys. Res., Sect. A **710**, 98–100 (2013).
5. A. Schindler, T. Hänsel, F. Frost, R. Fechner, A. Nickel, H.-J. Thomas, H. Neumann, and D. Hirsch, "Ion beam finishing technology for high precision optics production," in *Optical Fabrication and Testing* (2002), paper OTuB5.
6. T. Wang, L. Huang, M. Vescovi, D. Kuhne, K. Tayabaly, N. Bouet, and M. Idir, "Study on an effective one-dimensional ion-beam figuring method," Opt. Express **27**, 15368–15381 (2019).
7. L. Zhou, L. Huang, N. Bouet, K. Kaznatcheev, M. Vescovi, Y. Dai, S. Li, and M. Idir, "New figuring model based on surface slope profile for grazing-incidence reflective optics," J. Synchrotron Radiat. **23**, 1087–1090 (2016).

8. L. Zhou, M. Idir, N. Bouet, K. Kaznatcheev, L. Huang, M. Vescovi, Y. Dai, and S. Li, "One-dimensional ion-beam figuring for grazing-incidence reflective optics," J. Synchrotron Radiat. **23**, 182–186 (2016).

9. M. Hand, S. G. Alcock, M. Hillman, R. Littlewood, S. Moriconi, H. Wang, and K. Sawhney, "Ion beam figuring and optical metrology system for synchrotron x-ray mirrors," Proc. SPIE **11109**, 111090A (2019).

10. R. Conley, N. Bouet, J. Biancarosa, Q. Shen, L. Boas, J. Feraca, and L. Rosenbaum, "The NSLS-ii multilayer Laue lens deposition system," Proc. SPIE **7448**, 74480U (2009).

11. C. L. Carnal, C. M. Egert, and K. W. Hylton, "Advanced matrix-based algorithm for ion-beam milling of optical components," Proc. SPIE **1752**, 54–63 (1992).

12. J. F. Wu, Z. W. Lu, H. X. Zhang, and T. S. Wang, "Dwell time algorithm in ion beam figuring," Appl. Opt. **48**, 3930–3937 (2009).

13. C. Jiao, S. Li, and X. Xie, "Algorithm for ion beam figuring of low-gradient mirrors," Appl. Opt. **48**, 4090–4096 (2009).

14. S. Wilson and J. McNeil, "Neutral ion beam figuring of large optical surfaces," Proc. SPIE **818**, 320–325 (1987).

15. T. Wang, L. Huang, H. Kang, H. Choi, D. W. Kim, K. Tayabaly, and M. Idir, "RIFTA: a robust iterative Fourier transform-based dwell time algorithm for ion beam figuring," Sci. Rep. (to be published).

16. T. Wang, L. Huang, K. Tayabaly, and M. Idir, "Study on the performances of dwell time algorithms in ion beam figuring," Proc. SPIE **11175**, 111750M (2019).

17. L. Zhou, X. Xie, Y. Dai, C. Jiao, and S. Li, "Ion beam figuring system in NUDT," Proc. SPIE **6722**, 67224A (2007).

18. L. Zhou, Y.-F. Dai, X.-H. Xie, C.-J. Jiao, and S.-Y. Li, "Model and method to determine dwell time in ion beam figuring," Nanotechnol. Precis. Eng. **5**, 107–112 (2007).

19. Z. Yifan and J. C. L. Shengyi, "Realization of velocity mode in flat optics machining using ion beam," J. Mech. Eng. **45**, 152–156 (2009).

20. L. Huang, T. Wang, K. Tayabaly, D. Kuhne, W. Xu, W. Xu, M. Vescovi, and M. Idir, "Stitching interferometry for synchrotron mirror metrology at National Synchrotron Light Source II (NSLS-II)," Opt. Laser Eng. **124**, 105795 (2020).